Equivalent chassis-based model predictive control for three-axle trucks during tire blowout on expressway

Chao Fang
Dalian University of Technology
Ming Yue (yueming@dlut.edu.cn)
Dalian University of Technology https://orcid.org/0000-0002-2984-4659
Jinyong Shangguan
Dalian University of Technology
Lie Guo
Dalian University of Technology

Research Article

Keywords: Tire blowout, Equivalent chassis, Rollover stability maintenance, Model predictive control (MPC), Co-simulation platform

Posted Date: June 2nd, 2022

DOI: https://doi.org/10.21203/rs.3.rs-1657880/v1

Noname manuscript No.
(will be inserted by the editor)

Equivalent chassis-based model predictive control for three-axle trucks during tire blowout on expressway

Chao Fang · Ming Yue · Jinyong Shangguan · Lie Guo

Received: date / Accepted: date

Abstract Unexpected tire blowout on expressway is one of the most dangerous scenarios for heavy load multi-axle trucks, especially under the inexperienced driver's improper intervention. To this end, this paper proposes an autonomous tire blowout controller for three-axle trucks based on model predictive control (MPC) method. First of all, aiming at balancing the computing load and the path tracking accuracy, an equivalent chassis is transformed based on the stable two-dimensional vehicle dynamic model. Secondly, a tire blowout oriented vehicle high-fidelity dynamic model is established based on the equivalent chassis, in which the vehicle lateral, yaw and roll motion are all considered at the same time. Then, an MPC-based dynamic control strategy is proposed to achieve effective tire blowout suppression with consideration of vehicle rollover stability. Afterwards, a transient vertical tire force shock is employed to simulate the real tire blowout behavior, upon which two typical scenarios are constructed based on the TruckSim/Simulink co-simulation platform. The simulation results illustrate the feasibility and effectiveness of the proposed method.

Keywords Tire blowout · Equivalent chassis · Rollover stability maintenance · Model predictive control (MPC) · Co-simulation platform

C. Fang, M. Yue, J. Shangguan and L. Guo are with the School of Automotive Engineering, Dalian University of Technology, Dalian 116024, China; M. Yue and L. Guo are with the NingBo Institute of Dalian University of Technology, Ningbo 315000, China.
E-mail: yueming@dlut.edu.cn

1 Introduction

With the rapid development of industrial transportation, multi-axle heavy duty trucks play a more and more important role due to their massive load carrying capacity, high economic efficiency, rapid transportation speed, and so on, see e.g. [1–6] and the references therein. In addition to these unique characteristics, the mature modern automobile industry has also provided such kind of vehicles considerable ability to deal with extreme working situations. However, unexpected tire blowout on expressway, as a common extreme situation, which leads usually to terrible traffic accidents and property losses, is still a well-known complicated scenario waiting for further investigation in the vehicle control community [7–9].

To realise effective vehicle dynamic control subject to tire blowout on expressway, establishing a suitable dynamic model is the primary task. Recent researches about high-fidelity dynamic modeling method for multi-axle vehicles can be divided into two major categories based on their different ways of handling the multi-axle dynamics: establishing a three-axle model directly or establishing a two-axle model based on the equivalent chassis [10, 11]. Aiming at the problem of modeling directly for multi-axle vehicles, Jin et al [12] established a six DOF (Degree of freedom) vehicle dynamic model, including lateral, yaw and roll motion, as well as both the sprung and unsprung mass being considered, respectively. Meanwhile, Ref. [13] established a rigid multi-body system by applying the principle laws of the physical and mechanics directly for multi-axle bus automatic operating. These two classic dynamic models are both verified to be high-fidelity through the TruckSim software platform. However, their real-time performance cannot be well guaranteed due to their high

complexity. Therefore, more and more attention has been paid to the simplification of the dynamic modeling process for multi-axle vehicles recently to better balance the calculation load and the model accuracy. For instance, based on the modeling conventions of two-axle bicycle model, Williams [14] proposed a novel equivalent wheelbase for three-axle vehicles by solving the steady-state dynamic equations. The characteristics of the equivalent wheelbase agree well with the results originated from both the equivalent axle-moment method and the geometric method. Further, in order to make the modeling process more universal, Zhang et al [15] summarised several classical previous studies about dynamic equivalence, including D.E.Williams, Winkler-Gillespie and J.R.Ellis, and then, proposed an approximately equivalent and optimal method, which can be expediently used without formulating for every single case respectively. However, although many researchers have already studied the dynamic modeling process for multi-axle vehicles, there exist few investigations that take both the multi-axle dynamics equivalence and the vehicle rollover stability maintenance into consideration simultaneously while modeling, which motivates this study.

On the other hand, realising effective vehicle dynamic control in the presence of unexpected tire blowout on expressway is also in urgent requirement, especially for three-axle heavy load trucks [16, 17]. Generally, there are several well-known classic feasible and effective control methods in the vehicle control community, including model predictive control (MPC) [4, 18], sliding mode control (SMC) [19, 20], fuzzy control [21, 22], deep learning approach [23, 24], and so on. Among them, MPC has been used widely in the field of vehicle control due to its outstanding advantages such as rolling optimization and strong robustness over the past decades [25–27]. For example, Refs.[28–30] proposed an autonomous hazard escaping trajectory planning/tracking control framework for vehicles subject to tire blowout on expressway based on MPC theory, respectively. Simulation results exhibit both the rear-end collision avoidance and dynamic constraints were implemented successfully. Moreover, in [31], aiming at handling the tire blowout accident of electric vehicles with external disturbances such as crosswinds and road changes, a directional stability control method based on robust model predictive technology was proposed. This method has better maneuverability performance than traditional MPC, and it can improve the directional stability of the vehicle after a tire blowout on curved highway. Besides, to further consider the vehicle roll constraint in the control process, Liu et al [32] proposed an MPC-based scheme for high-speed autonomous ground vehicles stability control considering the influence of road terrain. However, there exists no further discussion about the vehicle rollover stability maintenance ability. In general, although many recent researches about vehicle control have been conducted based on the MPC method, there seems to be few discussions on maintaining the rollover stability of multi-axle trucks while performing trajectory tracking, especially in the case of unexpected tire blowout. Therefore, this study proposed an MPC-based vehicle controller, in which the vehicle lateral motion, yaw motion and rollover motion are all taken into consideration simultaneously in order to maximize the stability of the truck during tire blowout on expressway.

Consequently, in light of the benefits and limitations of these existing researches, this study attempts to propose an equivalent chassis-based model predictive control method for three-axle trucks during tire blowout on expressway. First of all, the equivalent two-axle chassis of the three-axle truck is established based on the stable vehicle dynamic model, where the equivalent rear axle cornering stiffness and the equivalent wheelbase are both obtained simultaneously. Accordingly, a tire blowout oriented full vehicle dynamic model including lateral motion, yaw motion and roll motion is constructed at the same time. Based on the equivalent vehicle dynamic model, an MPC-based vehicle controller is designed afterwards. Then, a large transient vertical tire force shock is employed to reflect the unexpected tire blowout behavior, upon which a TruckSim-Simulink co-simulation platform is constructed to verify the feasibility and the effectiveness of the proposed controller. Compared to the existing researches about tire blowout control of three-axle vehicles, the contributions of this paper yields twofold:

1. Aiming at overcoming the unexpected tire blowout scenario on expressway, a high-fidelity dynamic model of the three-axle truck is proposed, in which both the equivalent chassis characteristics and the vehicle rollover stability maintenance are taken into consideration simultaneously for the first time.
2. Based on the proposed equivalent dynamic model, a novel MPC-based control method aiming at tackling the hazard of tire blowout is designed, which can not only ensure the smoothness and accuracy of lane keeping, but also suppress the dangerous fluctuate of vehicle roll motion effectively at the same time.

The rest of this paper is organised as follows. Sect.2 mainly introduced the determination of the equivalent chassis and the tire blowout oriented high-fidelity vehicle dynamic model; In Sect.3, the MPC-based vehicle controller design process is outlined, as well as the s-

Table 1 Nomenclature

Notation	Description	Unit
ϕ	Roll angle	rad
φ	Yaw angle	rad
h	Height of CG	m
g	Gravitational constant	m/s^2
m	Mass of vehicle	kg
$\dot{x}$	Longitudinal speed	m/s
$\dot{y}$	Lateral speed	m/s
D_ϕ	Equivalent roll angular damping	Nm/(rad/s)
K_ϕ	Equivalent roll angular stiffness	Nm/rad
X	Longitudinal position in $\sum XOY$	m
Y	Lateral position in $\sum XOY$	m
a_y	Vehicle lateral acceleration	m/s^2
I_z	Moment inertia about the yaw axis	kgm^2
I_x	Moment inertia about the roll axis	kgm^2
δ_f	Front wheel steering angle	rad
l_e	Equivalent wheelbase	m
l_f/l_r	Equivalent distance of the front/rear axle from CG	m
$a/b/c$	Distance of the front/middle/rear axle from CG	m
$C_{\alpha re}$	Equivalent cornering stiffness of the middle and rear tires	N/rad
$C_{\alpha f}/C_{\alpha m}$ /$C_{\alpha r}$	Cornering stiffness of the front/middle/rear tires	N/rad

tandard quadratic programming formulation being exhibited; The tire blowout behavior simulation and two typical scenarios are presented in Sect.4 based on the TruckSim/Simulink co-simulation platform, followed by a brief conclusion in Sect.5.

2 Three-axle Truck Dynamics Modeling

Given the exclusive complexity of typical three-axle trucks, such as multi-axle dynamics, heavy load, long wheelbase, and so on, it is necessary to build a high-fidelity dynamic model under appropriate assumptions to realise effective control. First of all, the nomenclature of the major parameters used are shown in Tab.1.

2.1 Determination of the equivalent chassis

For a typical three-axle truck, as show in Fig.1, its middle and rear axles are usually very close and on the same side of the CG (Center of gravity). Meanwhile, the structure of the suspensions and the type of the tires used in these two axles are usually the same. Therefore, the middle and the rear axles can be regarded as an equivalent rear axle. Specially, the steering effect of a conventional two-axle vehicle is mainly dominated by the wheelbase and the cornering stiffness of tires, which are the two target equivalent parameters in this part as well. Furthermore, given that the sprung mass

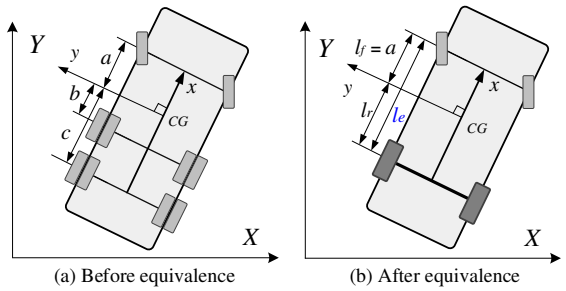

Fig. 1 Equivalent model of the three-axle truck.

plus load of heavy-duty truck is much greater than the unsprung mass, this study will no longer consider the sprung mass and the unsprung mass separately. Meanwhile, it's worth mentioning that in order to make it easier to calculate the relevant vehicle parameters such as the position of CG, the vehicle load mass is set to be equal to the unloaded vehicle mass.

As shown in Fig.1, the two tires on the left (right) side of the middle (rear) axle are firstly assumed to be one equivalent tire to reduce the calculation load. After that, a two DOF single track dynamic model is established firstly for the sake of equivalence, as shown in Fig.2(a), which can be written as

$$\begin{cases} m(\ddot{y} + \dot{x}\dot{\varphi} - h\ddot{\phi}\cos(\phi)) = 2F_{yf}\cos\delta_f + 2F_{ym} + 2F_{yr} \\ I_z\ddot{\varphi} = 2aF_{yf}\cos\delta_f - 2bF_{ym} - 2cF_{yr} \end{cases} \tag{1}$$

where F_{yf}, F_{ym} and F_{yr} represent the lateral forces of the front, middle and rear tires, respectively.

Under the assumptions of small angle and linear tire forces, lateral forces of tires on different axles can be expressed as

$$\begin{cases} F_{yf} = C_{\alpha f}(\delta_f - \dfrac{a\dot{\varphi} + \dot{y}}{\dot{x}}) \\ F_{ym} = C_{\alpha m}\ \dfrac{b\dot{\varphi} - \dot{y}}{\dot{x}} \\ F_{yr} = C_{\alpha r}\ \dfrac{c\dot{\varphi} - \dot{y}}{\dot{x}} \end{cases} \tag{2}$$

The equivalent process is assumed to be conducted under a steady state, so that $\ddot{y}, \ddot{\varphi}, \phi$ and $\ddot{\phi}$ are all set to be zero. Therefore, the single-track model (1) can be expressed as

$$\begin{bmatrix} \dfrac{\dot{y}}{\delta_f} & \dfrac{\dot{\varphi}}{\delta_f} \end{bmatrix}^T = -A_e^{-1}B_e \tag{3}$$

where

$$B_e = \begin{bmatrix} \dfrac{2C_{\alpha f}}{m} & \dfrac{2aC_{\alpha f}}{I_z} \end{bmatrix}^T$$

$$A_e = \begin{bmatrix} A_{e11} & A_{e12} \\ A_{e21} & A_{e22} \end{bmatrix}$$

with

$$\begin{cases} A_{e11} = -\dfrac{2}{m\dot{x}}(C_{\alpha f} + C_{\alpha m} + C_{\alpha r}) \\ A_{e12} = -\dot{x} - \dfrac{2}{m\dot{x}}(aC_{\alpha f} - bC_{\alpha m} - cC_{\alpha r}) \\ A_{e21} = -\dfrac{2}{I_z\dot{x}}(aC_{\alpha f} - bC_{\alpha m} - cC_{\alpha r}) \\ A_{e22} = -\dfrac{2}{I_z\dot{x}}(a^2C_{\alpha f} + b^2C_{\alpha m} + c^2C_{\alpha r}) \end{cases}$$

According to Refs.[14, 33], the yaw rate response under unit steering angle input of conventional two-axle vehicles can be expressed as

$$\frac{\dot{\varphi}}{\delta_f} = \frac{\dot{x}}{l_e + \dot{x}^2 K_e} \tag{4}$$

where K_e is the understeering characteristic parameter, which can be expressed as

$$K_e = \frac{m(l_r C_{\alpha re} - l_f C_{\alpha f})}{l_e C_{\alpha f} C_{\alpha re}}$$

By comparing Eqs.(3)-(4), the equivalent wheelbase l_e and the equivalent cornering stiffness of rear axle $C_{\alpha re}$ can be obtained as Eq.(5). More details about the process can be found in [12].

$$\begin{cases} l_e = \dfrac{C_{\alpha f}C_{\alpha r}(a+c)^2 + C_{\alpha m}C_{\alpha r}(b-c)^2 + C_{\alpha f}C_{\alpha m}(a+b)^2}{C_{\alpha f}\left[C_{\alpha m}(a+b) + C_{\alpha r}(a+c)\right]} \\ l_f = a\,, \quad l_r = l_e - l_f \\ K_e = \dfrac{m(bC_{\alpha m} + cC_{\alpha r} - aC_{\alpha f})}{C_{\alpha f}\left[C_{\alpha m}(a+b) + C_{\alpha r}(a+c)\right]} \\ C_{\alpha re} = \dfrac{ml_f C_{\alpha f}}{m(l_e - l_f) - K_e C_{\alpha f} l_e} \end{cases} \tag{5}$$

Remark 1 : Notice that the two target equivalent parameters l_e and $C_{\alpha re}$ are obtained simultaneously by now, upon which the full vehicle dynamic model can be established afterwards.

2.2 Rollover oriented vehicle dynamic model

Since the three-axle trucks are usually heavily loaded and have higher CG altitude, it needs to take the rollover stability maintenance into consideration while modeling [34, 35], as shown in Fig.2(b), which can be written as

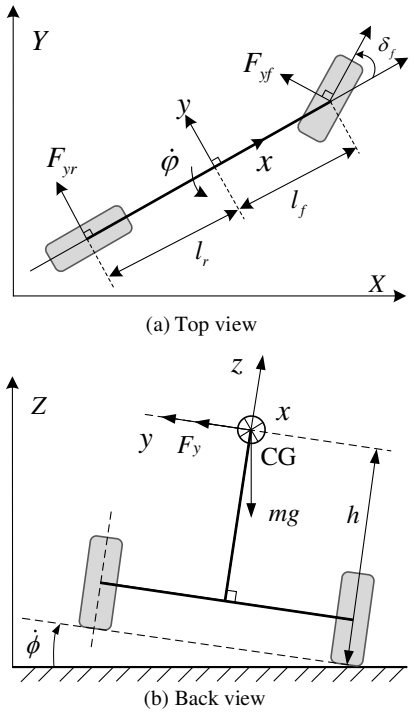

Fig. 2 Vehicle dynamic model.

$$I_x\ddot{\phi} = ma_y h + mgh\sin\phi - M_x \tag{6}$$

where M_x is the roll resistance moment generated by the suspension system, which can be expressed as $M_x = K_\phi\phi + D_\phi\dot{\phi}$.

By substituting Eq.(2) into Eq.(1) and Eq.(6), the equivalent two-axle vehicle dynamic model can be specifically expressed as

$$\begin{cases} \ddot{y} = -2\dot{y}(\dfrac{1}{m} + \dfrac{h^2}{I_x})(C_{\alpha f} + C_{\alpha re})\dfrac{1}{\dot{x}} \\ \qquad + \dot{\varphi}\left[2(\dfrac{1}{m} + \dfrac{h^2}{I_x})(l_r C_{\alpha re} - l_f C_{\alpha f})\dfrac{1}{\dot{x}} - \dot{x}\right] \\ \qquad - \phi\dfrac{hK_\phi}{I_x} - \dot{\phi}\dfrac{hD_\phi}{I_x} + 2\delta_f(\dfrac{1}{m} + \dfrac{h^2}{I_x})C_{\alpha f} \\ \ddot{\varphi} = 2\dot{y}\ \dfrac{l_r C_{\alpha re} - l_f C_{\alpha f}}{\dot{x}I_z} - 2\dot{\varphi}\ \dfrac{l_f^2 C_{\alpha f} + l_r^2 C_{\alpha re}}{\dot{x}I_z} \\ \qquad + 2\delta_f\ \dfrac{l_f C_{\alpha f}}{I_z} \\ \ddot{\phi} = -2\dot{y}h\ \dfrac{C_{\alpha f} + C_{\alpha re}}{I_x\dot{x}}\ + 2\dot{\varphi}h\ \dfrac{C_{\alpha re}l_r - C_{\alpha f}l_f}{I_x\dot{x}} \\ \qquad - \phi\ \dfrac{K_\phi}{I_x} - \dot{\phi}\ \dfrac{D_\phi}{I_x} + 2\delta_f h\ \dfrac{C_{\alpha f}}{I_x} \\ \dot{X} = \dot{x}\cos\varphi - \dot{y}\sin\varphi \\ \dot{Y} = \dot{x}\sin\varphi + \dot{y}\cos\varphi \end{cases} \tag{7}$$

2.3 Rollover oriented stability index

According to the existing studies [15, 36], lateral load transfer rate (LTR) is well known as a reliable index to evaluate vehicle rollover risk. Conventional LTR index definition can be written as

$$LTR = \frac{F_L - F_R}{F_L + F_R} \tag{8}$$

where F_L and F_R are the vehicle load on the left and right side, respectively. Obviously, the value of LTR belongs to [-1, 1]. Meanwhile, the higher absolute value of LTR, the greater the vehicle rollover risk.

However, F_L and F_R cannot be measured directly by sensors in practice, so that the conventional LTR index usually needs to be estimated online based on the vehicle dynamic model presented above, as follows

$$LTR_d = \frac{2}{mgT_w}(I_x\ddot{\phi} - mga_y - mgh\phi) = \boldsymbol{E}_1\boldsymbol{\xi} + \boldsymbol{E}_2\dot{\boldsymbol{\xi}} \tag{9}$$

where

$$\begin{cases} \boldsymbol{E}_1 = [\quad 0 \quad 0 \quad -\dfrac{2h\dot{x}}{gT_w} \quad -\dfrac{2h}{T_w} \quad 0 \quad 0 \quad 0 \quad] \\ \boldsymbol{E}_2 = [-\dfrac{2h}{gT_w} \quad 0 \quad 0 \quad 0 \quad 2\,\dfrac{I_x + mh^2}{mgT_w} \quad 0 \quad 0 \quad] \end{cases}$$

where T_w is the vehicle track; $\boldsymbol{\xi} = \left[\dot{y}, \varphi, \dot{\varphi}, \phi, \dot{\phi}, X, Y\right]^T$ is set to be the system state vector.

This new LTR index is now available to be used in estimating the rollover risk for heavy-duty trucks [37].

3 MPC-based Control Strategy

In this section, the MPC-based controller with multi-constrains is proposed to tackle the tire blowout hazard for three-axle trucks for the first time. The schematic diagram of the control system is shown in Fig.3. As shown, the whole control system can be divided into three major parts, which are the vehicle dynamic model, the vehicle dynamic control and the tire blowout simulation, respectively. First of all, in the vehicle dynamic model part, the equivalent two-axle chassis of the three-axle truck is established, upon which a full vehicle dynamic model including lateral motion, yaw motion and roll motion is constructed accordingly. After that, in the vehicle dynamic control module, the MPC-based controller is particularly designed, as well as the single lane change reference path being exhibited. Then, a large transient vertical tire force shock is employed to reflect the unexpected tire blowout behavior, which is exported to the front-left tire in the TruckSim software afterwards. Meanwhile, a TruckSim-Simulink co-simulation platform is constructed to verify the feasibility and the effectiveness of the proposed controller, which is presented in the tire blowout simulation module.

3.1 MPC-based controller formulation

To balance the calculation load and the control effectiveness, the complicated dynamic model (7) has to be simplified to satisfy the requirement. Firstly, $\boldsymbol{\xi} = \left[\dot{y}, \varphi, \dot{\varphi}, \phi, \dot{\phi}, X, Y\right]^T$ is set to be the system state vector as mentioned above, while the front wheel steering angle δ_f is set to be the control input $\boldsymbol{u}$, that is $\boldsymbol{u} = [\delta_f]$. After that, the system output is set to be $\boldsymbol{\eta} = [\varphi, \phi, X, Y]^T$. The state-form of the vehicle dynamic model can be written as

$$\begin{cases} \dot{\boldsymbol{\xi}} = f(\boldsymbol{\xi}, \boldsymbol{u}) \\ \boldsymbol{\eta} = \boldsymbol{C}\boldsymbol{\xi} \end{cases} \tag{10}$$

where

$$\boldsymbol{C} = \begin{bmatrix} 0&1&0&0&0&0&0 \\ 0&0&0&1&0&0&0 \\ 0&0&0&0&0&1&0 \\ 0&0&0&0&0&0&1 \end{bmatrix}$$

First of all, the dynamic system has to be discretized in order to realise effective controller design, as follows

$$\begin{cases} \boldsymbol{\xi}(t+1) = \boldsymbol{\xi}(t) + T\dot{\boldsymbol{\xi}}(t) = F(\boldsymbol{\xi}(t), \boldsymbol{u}_t) \\ \quad \boldsymbol{\eta}(t) = \boldsymbol{C}\boldsymbol{\xi}(t) \end{cases} \tag{11}$$

where T is the sampling time.

After discretizing, the system is still too complicated to realise real-time control, let alone the dynamic constraints. Therefore, to further linearize the proposed system, the current working point of the control system is assumed to be $[\boldsymbol{\xi}_0, \boldsymbol{u}_0]$. Meanwhile, $\hat{\boldsymbol{\xi}}_0(k)$ is set to be the system status under the constant control signal $\boldsymbol{u}_0$, which can be written as

$$\begin{cases} \quad \boldsymbol{u}(k) = \boldsymbol{u}_0 \\ \quad \hat{\boldsymbol{\xi}}_0(0) = \boldsymbol{\xi}_0 \\ \hat{\boldsymbol{\xi}}_0(k+1) = F(\hat{\boldsymbol{\xi}}_0(k), \boldsymbol{u}(k)) \end{cases} \tag{12}$$

Next, the Eq.(11) is expanded using the first-order Taylor expansion method, as follows

$$\begin{aligned} \boldsymbol{\xi}(k+1) = \hat{\boldsymbol{\xi}}_0(k+1) + \boldsymbol{A}_{k,0}\left[\boldsymbol{\xi}(k) - \hat{\boldsymbol{\xi}}_0(k)\right] \\ + \boldsymbol{B}_{k,0}\left[\boldsymbol{u}(k) - \boldsymbol{u}_0\right] \end{aligned} \tag{13}$$

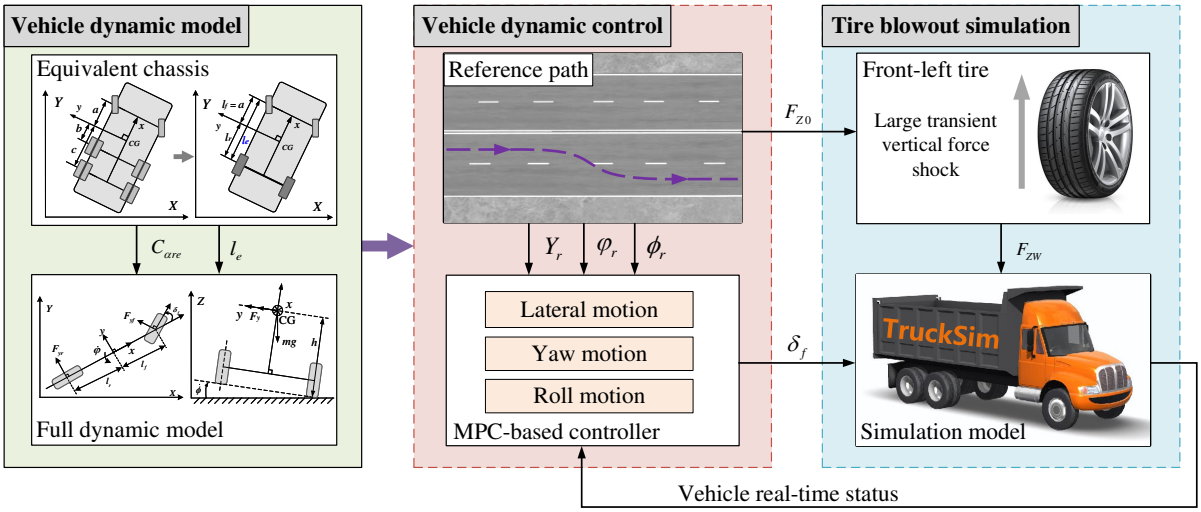

Fig. 3 Schematic diagram of the control system.

where

$$\boldsymbol{A}_{k,0} = \frac{\partial F}{\partial \boldsymbol{\xi}}|_{\hat{\boldsymbol{\xi}}_0(k),\boldsymbol{u}_0} = \begin{bmatrix} A_{11} & 0 & A_{13} & A_{14} & A_{15} & 0 & 0 \\ 0 & 1 & T & 0 & 0 & 0 & 0 \\ A_{31} & 0 & A_{33} & 0 & 0 & 0 & 0 \\ 0 & 0 & 0 & 1 & T & 0 & 0 \\ A_{51} & 0 & A_{53} & A_{54} & A_{55} & 0 & 0 \\ A_{61} & A_{62} & 0 & 0 & 0 & 1 & 0 \\ A_{71} & A_{72} & 0 & 0 & 0 & 0 & 1 \end{bmatrix}$$

$$\boldsymbol{B}_{k,0} = \frac{\partial F}{\partial \boldsymbol{u}_0}|_{\hat{\boldsymbol{\xi}}_0(k),\boldsymbol{u}_0} = \begin{bmatrix} B_1 & 0 & B_3 & 0 & B_5 & 0 & 0 \end{bmatrix}^T$$

with

$$A_{11} = 1 - 2T(C_{\alpha f} + C_{\alpha re})(\frac{1}{m} + \frac{h^2}{I_x})\frac{1}{\dot{x}}$$

$$A_{13} = T\left[2(C_{\alpha re}l_r - C_{\alpha f}l_f)(\frac{1}{m} + \frac{h^2}{I_x})\frac{1}{\dot{x}} - \dot{x}\right]$$

$$A_{31} = 2T\frac{(C_{\alpha re}l_r - C_{\alpha f}l_f)}{I_z\dot{x}} \qquad A_{51} = -2Th\frac{C_{\alpha f} + C_{\alpha re}}{I_x\dot{x}}$$

$$A_{61} = -T\sin\varphi \qquad A_{71} = T\cos\varphi$$

$$A_{62} = -T(\dot{y}\cos\varphi + \dot{x}\sin\varphi) \qquad A_{72} = T(\dot{x}\cos\varphi - \dot{y}\sin\varphi)$$

$$A_{33} = 1 - 2T\frac{l_f^2C_{\alpha f} + l_r^2C_{\alpha re}}{\dot{x}I_z} \qquad A_{53} = 2Th\frac{C_{\alpha re}l_r - C_{\alpha f}l_f}{I_x\dot{x}}$$

$$A_{14} = -T(\frac{hK_\phi}{I_x}) \qquad A_{54} = -T\frac{K_\phi}{I_x}$$

$$A_{15} = -T\frac{D_\phi h}{I_x} \qquad A_{55} = 1 - T\frac{D_\phi}{I_x}$$

$$B_1 = 2TC_{\alpha f}(\frac{1}{m} + \frac{h^2}{I_x}) \qquad B_3 = 2T\frac{l_fC_{\alpha f}}{I_z}$$

$$B_5 = 2Th\frac{C_{\alpha f}}{I_x}$$

Further, Eq.(13) can be rewritten as follows

$$\boldsymbol{\xi}(k+1) = \boldsymbol{A}_{k,0}\boldsymbol{\xi}(k) + \boldsymbol{B}_{k,0}\boldsymbol{u}(k) + \boldsymbol{d}_{k,0} \tag{14}$$

where

$$\boldsymbol{d}_{k,0} = \hat{\boldsymbol{\xi}}_0(k+1) - \boldsymbol{A}_{k,0}\hat{\boldsymbol{\xi}}_0(k) - \boldsymbol{B}_{k,0}\boldsymbol{u}_0$$

After that, an augmented state of the system can be expressed as

$$\overline{\boldsymbol{\xi}}(k) = \begin{bmatrix} \boldsymbol{\xi}(k) \\ \boldsymbol{u}(k-1) \end{bmatrix} \tag{15}$$

Now, the MPC-based control system can be obtained by combing Eq.(14) with Eq.(15), as follows

$$\begin{cases} \overline{\boldsymbol{\xi}}(k+1) = \overline{\boldsymbol{A}}_{k,0}\overline{\boldsymbol{\xi}}(k) + \overline{\boldsymbol{B}}_{k,0}\Delta\boldsymbol{u}(k) + \overline{\boldsymbol{d}}_{k,0} \\ \overline{\boldsymbol{\eta}}(k) = \overline{\boldsymbol{C}}\ \overline{\boldsymbol{\xi}}(k) \end{cases} \tag{16}$$

where

$$\overline{\boldsymbol{A}}_{k,0} = \begin{bmatrix} \boldsymbol{A}_{k,0} & \boldsymbol{B}_{k,0} \\ 0 & 1 \end{bmatrix}, \qquad \overline{\boldsymbol{B}}_{k,0} = \begin{bmatrix} \boldsymbol{B}_{k,0} \\ 1 \end{bmatrix}$$

$$\overline{\boldsymbol{C}} = \begin{bmatrix} \boldsymbol{C} & \boldsymbol{0}_{4\times1} \end{bmatrix}, \qquad \overline{\boldsymbol{d}}_{k,0} = \begin{bmatrix} \boldsymbol{d}_{k,0} \\ 0 \end{bmatrix}$$

In order to simplify the calculation process, the matrixes $\bar{\boldsymbol{d}}_{k,t}$, $\bar{\boldsymbol{A}}_{k,t}$ and $\bar{\boldsymbol{B}}_{k,t}$ are all regarded as fixed value matrixes $\bar{\boldsymbol{d}}$, $\bar{\boldsymbol{A}}$ and $\bar{\boldsymbol{B}}$.

Ultimately, the expression of the output in the prediction time domain is as follows

$$\boldsymbol{Y}(t) = \boldsymbol{\Psi}\bar{\boldsymbol{\xi}}(t|t) + \boldsymbol{\Theta}\boldsymbol{\Delta U}(t) + \boldsymbol{\Gamma}\boldsymbol{\Phi} \tag{17}$$

where

$$\boldsymbol{Y}(t) = \begin{bmatrix} \overline{\boldsymbol{\eta}}(t+1|t) \\ \overline{\boldsymbol{\eta}}(t+2|t) \\ \cdots \\ \overline{\boldsymbol{\eta}}(t+N_c|t) \\ \cdots \\ \overline{\boldsymbol{\eta}}(t+N_p|t) \end{bmatrix}_{N_p\times 1}, \ \boldsymbol{\Psi} = \begin{bmatrix} \bar{\boldsymbol{C}}\bar{\boldsymbol{A}} \\ \bar{\boldsymbol{C}}\bar{\boldsymbol{A}}^2 \\ \cdots \\ \bar{\boldsymbol{C}}\bar{\boldsymbol{A}}^{N_c} \\ \cdots \\ \bar{\boldsymbol{C}}\bar{\boldsymbol{A}}^{N_p} \end{bmatrix}_{N_p\times 1}$$

$$\boldsymbol{\Delta U}(t) = \begin{bmatrix} \boldsymbol{\Delta u}(t|t) \\ \boldsymbol{\Delta u}(t+1|t) \\ \cdots \\ \boldsymbol{\Delta u}(t+N_c-1|t) \end{bmatrix}_{N_c\times 1}, \ \boldsymbol{\Phi} = \begin{bmatrix} \bar{\boldsymbol{d}} \\ \bar{\boldsymbol{d}} \\ \cdots \\ \bar{\boldsymbol{d}} \\ \cdots \\ \bar{\boldsymbol{d}} \end{bmatrix}_{N_p\times 1}$$

$$\boldsymbol{\Theta} = \begin{bmatrix} \bar{\boldsymbol{C}}\bar{\boldsymbol{B}} & \boldsymbol{0}_{4\times 1} & \cdots & \boldsymbol{0}_{4\times 1} \\ \bar{\boldsymbol{C}}\bar{\boldsymbol{A}}\bar{\boldsymbol{B}} & \bar{\boldsymbol{C}}\bar{\boldsymbol{B}} & \cdots & \boldsymbol{0}_{4\times 1} \\ \vdots & \vdots & \ddots & \vdots \\ \bar{\boldsymbol{C}}\bar{\boldsymbol{A}}^{N_p-1}\bar{\boldsymbol{B}} & \bar{\boldsymbol{C}}\bar{\boldsymbol{A}}^{N_p-2}\bar{\boldsymbol{B}} & \cdots & \bar{\boldsymbol{C}}\bar{\boldsymbol{A}}^{N_p-N_c}\bar{\boldsymbol{B}} \end{bmatrix}_{N_p\times N_c}$$

$$\boldsymbol{\Gamma} = \begin{bmatrix} \bar{\boldsymbol{C}} & \boldsymbol{0}_{4\times 8} & \cdots & \boldsymbol{0}_{4\times 8} \\ \bar{\boldsymbol{C}}\bar{\boldsymbol{A}} & \bar{\boldsymbol{C}} & \cdots & \boldsymbol{0}_{4\times 8} \\ \vdots & \vdots & \ddots & \vdots \\ \bar{\boldsymbol{C}}\bar{\boldsymbol{A}}^{N_p-1} & \bar{\boldsymbol{C}}\bar{\boldsymbol{A}}^{N_p-2} & \cdots & \bar{\boldsymbol{C}} \end{bmatrix}_{N_p\times N_p}$$

where N_p and N_c represent the predictive and the control horizon in the vehicle dynamic control module, respectively.

The control sequence can be obtained by solving the cost function, in which the system output error, the control input constrains and the relaxation factor are all taken into consideration, respectively, as follows

$$\begin{aligned} \min \quad & \boldsymbol{\mathcal{J}}_t = \sum_{i=1}^{N_p} ||\boldsymbol{\eta}(k+i|t) - \boldsymbol{\eta}_{\text{ref}}(k+i|t)||_Q^2 \\ & + \sum_{i=0}^{N_c-1} ||\boldsymbol{\Delta u}(k+i|t)||_R^2 + \rho\varepsilon^2 \\ s.t. \quad & \boldsymbol{\Delta U}_{\min} \leqslant \boldsymbol{\Delta U} \leqslant \boldsymbol{\Delta U}_{\max} \\ & \boldsymbol{U}_{\min} \leqslant \boldsymbol{K}\boldsymbol{\Delta U} + \boldsymbol{U} \leqslant \boldsymbol{U}_{\max} \\ & \boldsymbol{Y}_{\min} \leqslant \boldsymbol{Y} \leqslant \boldsymbol{Y}_{\max} \\ & 0 \leqslant \varepsilon \leqslant \mathrm{M} \end{aligned} \tag{18}$$

where Q, R and ρ denote the weighting matric/index, respectively; ε stands for relaxation factor, whose value is positive; ΔU is control increment sequence, which equals to $\Delta U(t)$; U is the control sequence of the previous step, which equals to $1_{Nc} \bigotimes u(t-1)$; K is the Kronecker matrix, which can be expressed as

$$K = \underbrace{\begin{bmatrix} 1 & 0 & \cdots & \cdots & 0 \\ 1 & 1 & 0 & \cdots & 0 \\ 1 & 1 & 1 & \ddots & 0 \\ \vdots & \vdots & \ddots & \ddots & 0 \\ 1 & 1 & \cdots & 1 & 1 \end{bmatrix}}_{N_c\times N_c} \otimes 1.$$

3.2 Rollover stability oriented multi-constraints

In order to realise standard quadratic programming, the error between the system output with the reference state needs to be defined firstly, as follows

$$\boldsymbol{Y} - \boldsymbol{Y}_{ref} = \boldsymbol{E} + \boldsymbol{\Theta}\boldsymbol{\Delta U}(t) \tag{19}$$

where $\boldsymbol{E}$ is the error between the system response without control and the reference trajectory, which can be obtained by $\boldsymbol{E} = \boldsymbol{\Psi}\boldsymbol{\xi}(t|t) + \boldsymbol{\Gamma}\boldsymbol{\Phi} - \boldsymbol{Y}_{ref}$; $\boldsymbol{Y}_{ref}$ donates the given reference trajectory information.

Finally, the cost function of standard quadratic form can be expressed as

$$\begin{aligned} \min \quad \boldsymbol{\mathcal{J}}_t = & \frac{1}{2}\begin{bmatrix} \boldsymbol{\Delta U}(t) \\ \varepsilon \end{bmatrix}^T \begin{bmatrix} 2(\boldsymbol{\Theta}^T Q\ \boldsymbol{\Theta} + R) & 0 \\ 0 & 2\rho \end{bmatrix} \begin{bmatrix} \boldsymbol{\Delta U}(t) \\ \varepsilon \end{bmatrix} \\ & + \begin{bmatrix} 2\boldsymbol{E}^T Q\ \boldsymbol{\Theta} & 0 \end{bmatrix} \begin{bmatrix} \boldsymbol{\Delta U}(t) \\ \varepsilon \end{bmatrix} \end{aligned} \tag{20}$$

Meanwhile, the dynamic constrains can be written as

$$\begin{aligned} s.t. \quad & \begin{bmatrix} \boldsymbol{\Delta U}_{min} \\ 0 \end{bmatrix} \leqslant \begin{bmatrix} \boldsymbol{\Delta U}(t) \\ \varepsilon \end{bmatrix} \leqslant \begin{bmatrix} \boldsymbol{\Delta U}_{max} \\ \mathrm{M} \end{bmatrix} \\ & \begin{bmatrix} \boldsymbol{K} & -\boldsymbol{I}_{N_c\times 1} \\ -\boldsymbol{K} & -\boldsymbol{I}_{N_c\times 1} \\ \boldsymbol{\Theta} & \boldsymbol{0}_{N_c\times 1} \\ -\boldsymbol{\Theta} & \boldsymbol{0}_{N_c\times 1} \end{bmatrix} \begin{bmatrix} \boldsymbol{\Delta U}(t) \\ \varepsilon \end{bmatrix} \leqslant \begin{bmatrix} \mathbf{U}_{\max} - \mathrm{U} \\ -\mathbf{U}_{\min} + \mathrm{U} \\ \mathbf{Y}_{\max} - \Psi\boldsymbol{\xi} - \Gamma\Phi \\ -\mathbf{Y}_{\min} + \Psi\boldsymbol{\xi} + \Gamma\Phi \end{bmatrix} \end{aligned} \tag{21}$$

As a result, the control input $\boldsymbol{u}$, which equals to the steering angle at the previous moment plus the first element of the control sequence $\boldsymbol{\Delta U}$, can be ultimately obtained by solving the optimal function Eq.(20) with constrains Eq.(21), as follows

$$\boldsymbol{u}(t) = \boldsymbol{u}(t-1) + \boldsymbol{\Delta u}(t) \tag{22}$$

where $\boldsymbol{u}(t)$ is the required control input, that is the front wheel steering angle δ_f at each step.

Table 2 Relevant parameters and constraints

Parameters	Value	Parameters	Value
N_c	5	N_p	10
ρ	10^3	M	0.05
m	17050 kg	h	1.41 m
l_f	2.943 m	l_r	2.667 m
g	9.8 m/s^2	$\dot{x}$	20 m/s
Y_{min1}	-2.5 m	Y_{max1}	2.5 m
Y_{min2}	-2 m	Y_{max2}	350 m
X_{min1}	-2 m	X_{max1}	450 m
X_{min2}	-2.5 m	X_{max2}	250 m
u_{min}	-0.2616 rad	u_{max}	0.2616 rad
Δu_{min}	-0.0222 rad	Δu_{max}	0.0222 rad
$\varphi_{\min 1}$	-0.5 rad	$\varphi_{\max 1}$	0.5 rad
$\varphi_{\min 2}$	-0.1 rad	$\varphi_{\max 2}$	2 rad
$\phi_{\min}$	-0.1 rad	$\phi_{\max}$	0.1 rad
I_x	10431 Kg·m^2	I_z	28900 Kg·m^2
$C_{\alpha f}$	157560 N/rad	$C_{\alpha f}$	509610 N/rad
K_ϕ	378147 N·m/rad	D_ϕ	7815 N·s/rad
R	$5 \times 10^5 I_{N_u \times N_c}$	T	0.025 s

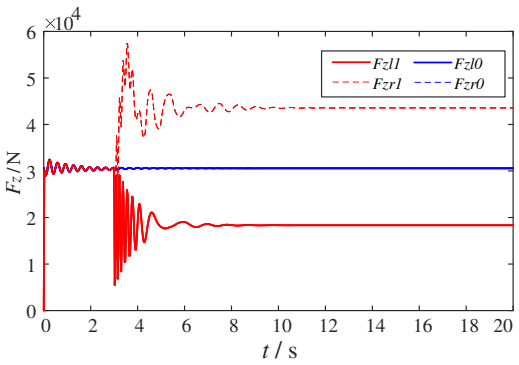

Fig. 4 Vertical front tire forces before/after blowout.

4 Simulation analysis

To validate the feasibility and the effectiveness of the proposed method, two typical scenarios are designed based on the TruckSim/Simulink co-simulation platform with the tire blowout behavior simulation being introduced firstly. Meanwhile, the key parameters characterizing the selected three-axle vehicle dynamics and the major parameters used in the MPC-based vehicle controller obtained by trial-and-error adjust method are shown in Tab.2, respectively.

4.1 Tire blowout behavior simulation

Given that there are few investigations about the tire blowout behavior simulation, it is necessary to figure out how to reproduce it in the simulation process firstly. Previous experimental researches show that many physical characteristics of a tire change suddenly after blowout, such as the rolling resistance coefficient, the longitudinal stiffness, the effective radius, etc. However,

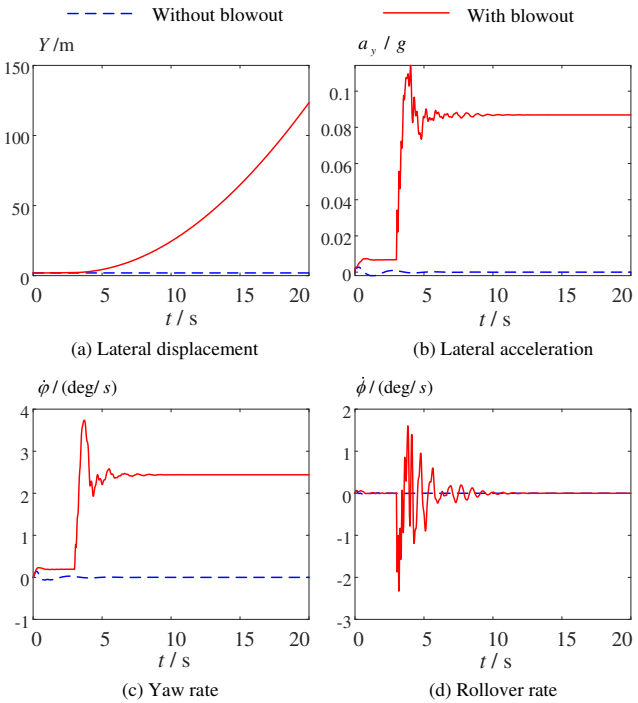

Fig. 5 Vehicle responses before/after blowout.

the dominant factor reflecting the mechanical properties of the burst tire is the vertical load redistribution, which leads easily to large transient fluctuation of the vertical force after blowout according to the literature [28]. Therefore, a large transient vertical shock force is employed in this study to describe the influence of tire blowout on expressway. Since the front wheels are the steering wheels, their blowout has a great negative influence on the vehicle stability. Consequently, blowout behavior is set to be applied on the front-left tire in this study. To be specifically, a TruckSim/Simulink co-simulation is performed firstly without any tire blowout to collect the normal front-left tire force data of the vehicle during the whole process. After that, a large transient vertical shock force is applied to the front-left tire based on the data set established above to simulate the tire blowout process, which can be expressed as

$$F_{zw} = \begin{cases} F_{zo} & \text{Before blowout} \\ 0.6F_{zo} - 5 \times 10^3 e^{1-t} \sin\left(20e^{(1-0.45t)}t\right) & \text{After blowout} \end{cases} \tag{23}$$

where F_{zw}/F_{zo} is the tire vertical force with/without the large transient vertical shock, respectively.

The comparison of the vertical tire forces with/without front-left tire blowout while driving along a straight lane is shown in Fig.4, where F_{zl1} and F_{zr1} donate

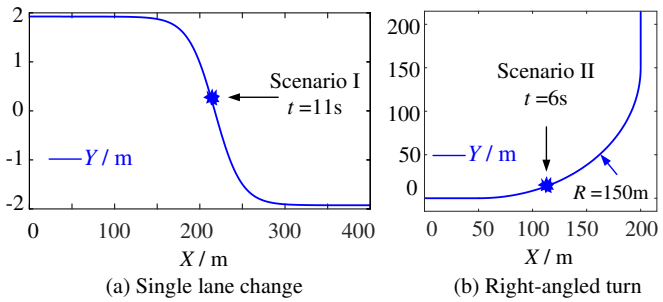

(a) Single lane change (b) Right-angled turn

Fig. 6 Reference trajectory curves.

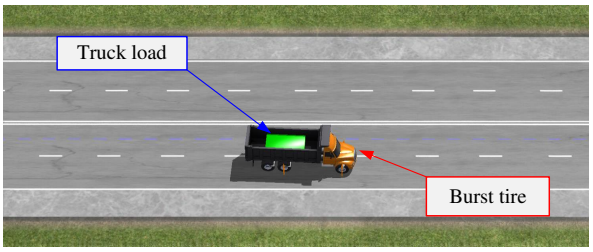

(a) Scenario I: Single lane change

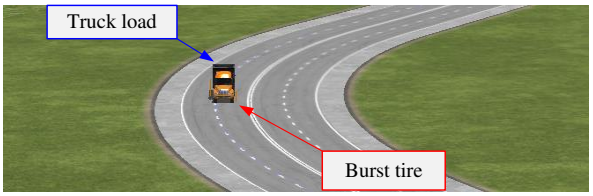

(b) Scenario II: Right-angled turn

Fig. 7 Simulation animations of different scenarios.

tire forces of front left/right tire with blowout, respectively, while F_{zl0} and F_{zr0} donate tire forces of front left/right tire without blowout, respectively. Meanwhile, the blowout of the front-left tire is set to be triggered at $t = 3$s. The responses of four typical related parameters including the lateral deviation, the lateral acceleration, the yaw rate and the rollover rate before/after tire blowout are depicted in Fig.5, respectively. As shown in the figure, without effective control, the vehicle would soon deviate from the expected trajectory, as well as both vehicle yaw rate and rollover rate would fluctuate greatly in varying degrees. Obviously, the trends of these curves are very similar to the simulation and experimental research results about tire blowout mechanism and influence presented in [28, 38–40]. Therefore, applying a transient vertical shock is a feasible way to realize high-fidelity tire blowout mechanism simulation to some extent.

4.2 Scenario I

To verify the effectiveness of the proposed control method, two typical maneuver scenarios are designed,

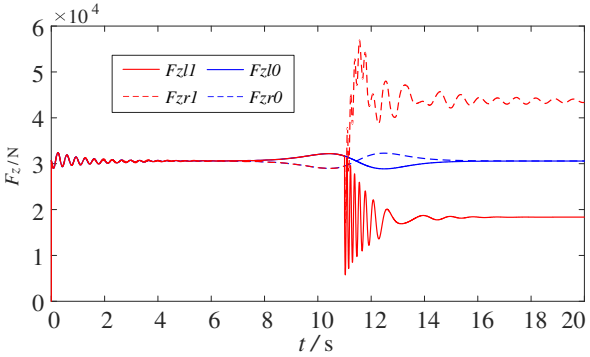

Fig. 8 Vertical front tire forces before/after blowout at t=11s.

including the single lane change maneuver and the right-angled turn maneuver. Both the reference trajectories are shown in Fig.6, respectively. Meanwhile, both the two different simulation scenario animations are exhibited in Fig.7, in which the tire blowout events are triggered at $t = 11$s and $t = 6$s, respectively. Specifically, it's worth mentioning that all the control results are presented in the form of comparisons of three curves, including the results from no blowout conditions and results from blowout conditions with/without vehicle rollover control, respectively.

In the single lane change scenario, the unexpected front-left tire blowout is set to be triggered during the process of maneuver at the time of $t = 11$s, as shown in Fig.6(a) and Fig.7(a). The vertical tire force responses with/without blowout simulation are shown in Fig.8, where the red curves donate the left/right tire forces under blowout condition, while the blue curves represent the front left/right tire forces originated from normal condition, respectively.

The vehicle responses of four different typical parameters after tire blowout are shown in Fig.9, where the green dashed curves represent the responses under no tire blowout condition, while the blue/red curves represent the tire blowout control results without/with consideration of vehicle rollover stability maintenance, respectively. First of all, it suggests that no matter the rollover stability is considered or not, the real vehicle motion trajectory can catch up with the reference trajectory after the front-left tire blowout is triggered, as shown in Fig.9(a). However, the vehicle lateral acceleration converges to zero faster once the rollover stability is considered in the controller, as show in Fig.9(b). Furthermore, the evolution law is even more evident in Fig.9(c) and Fig.9(d). Obviously, all of the curves would fluctuate in varying degrees suddenly after the blowout is triggered and converge to zero afterwards. However, when the tire blowout event is triggered at $t = 11$s, the yaw rate curve and the roll rate curve originated from

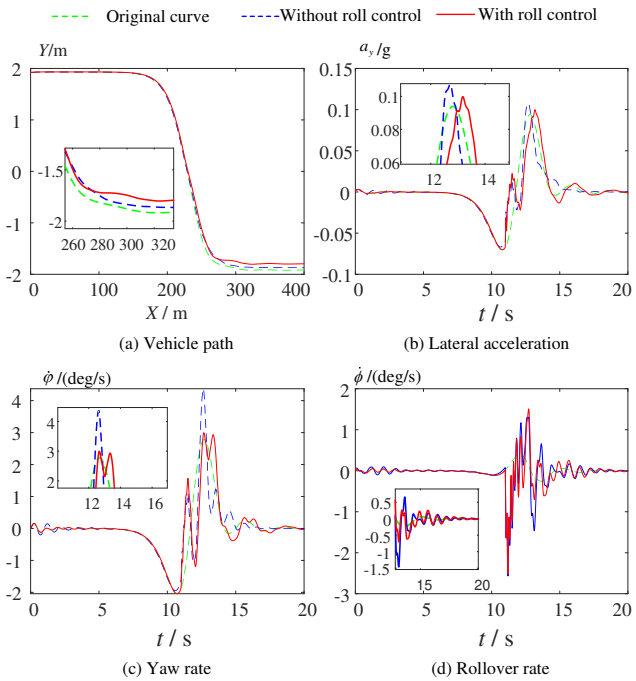

Fig. 9 Vehicle responses before/after blowout at t=11s.

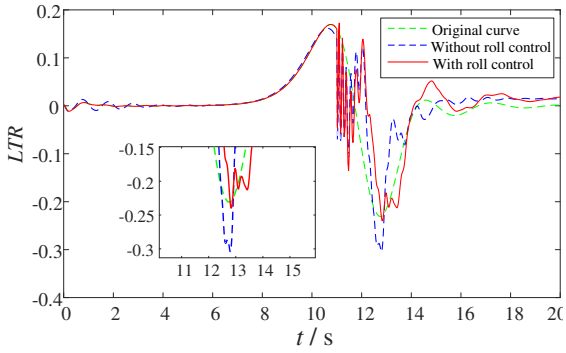

Fig. 10 LTR before/after blowout at t=11s.

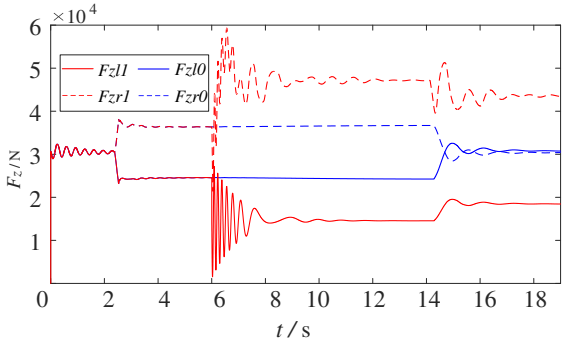

Fig. 11 Vertical front tire forces before/after blowout at t=6s.

the controller considering vehicle rollover stability oscillate more gently, while these originated from the other controller still have large oscillation amplitudes, which may lead to an increase of potential traffic accident risk. In this sense, considering vehicle rollover stability maintenance during the controller design process is not only necessary, but also effective.

To show the vehicle rollover risk more clearly, the vehicle LTR index curves under different controllers are depicted in Fig.10, respectively. Firstly, before tire blowout, the deviation among these three curves seems minor, which means both controllers satisfy the control requirements under normal conditions. However, after the blowout is triggered at t = 11s, the LTR curves originated from both controllers start fluctuating suddenly. Meanwhile, it's obvious that the red curve, which donates the LTR trend of the controller considering rollover stability, converges much faster than the blue curve. In other word, the vehicle status becomes much more stable and changes much more smoother while the rollover maintenance is involved in the controller, which once again validates the efficiency and effectiveness of the proposed method.

4.3 Scenario II

In order to further evaluate the adaptability of the proposed method under different working conditions, a right-angled turn reference path is particularly designed, of which the radius is 150m, as shown in Fig.6(b) and Fig.7(b). In this scenario, the unexpected tire blowout event is set to be triggered at t = 6s, and the corresponding vertical force curves of the front tires with/without blowout are shown in Fig.11, respectively.

The comparisons of four typical responses of vehicle motion characteristics, including the vehicle path, the lateral acceleration, the yaw rate and the rollover rate, are depicted in Fig.12, respectively. First of all, the errors between the three different curves in Fig.12(a) seems minor, which means the vehicle can achieve effective path tracking no matter the rollover stability is considered or not. Secondly, as the blowout is triggered at t = 6s, all of the curves in Fig.12(b), Fig.12(c) and Fig.12(d) start fluctuating in varying degrees suddenly. The difference lies in that the curves originated from the controller considering vehicle rollover stability converge more faster and smoother. The revolution law is much evident at around t = 14s, when the vehicle has almost finished the maneuver and return back to the straight lane. In a word, the performance of the controller increased evidently while the vehicle rollover stability is involved.

The LTR responses of the right-angled turn maneuver are depicted in Fig.13, respectively. As shown, due to the relatively high speed and the right-angled path, all the three curves go lower than −0.5 at the time

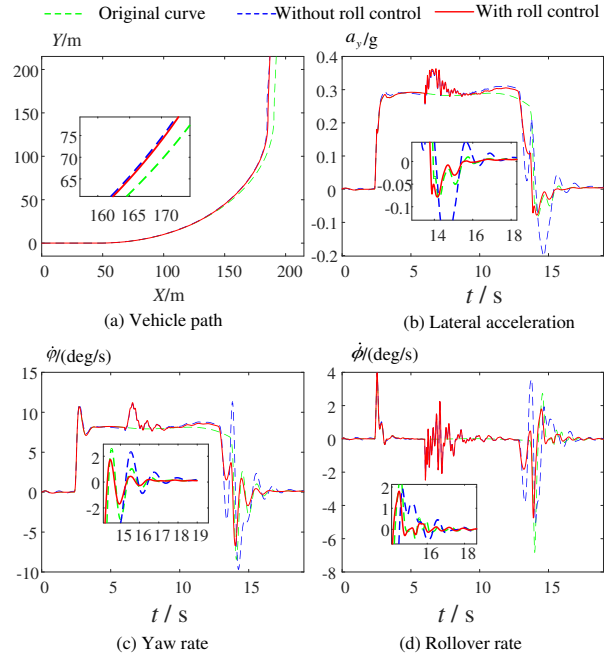

Fig. 12 Vehicle responses before/after blowout at t=6s.

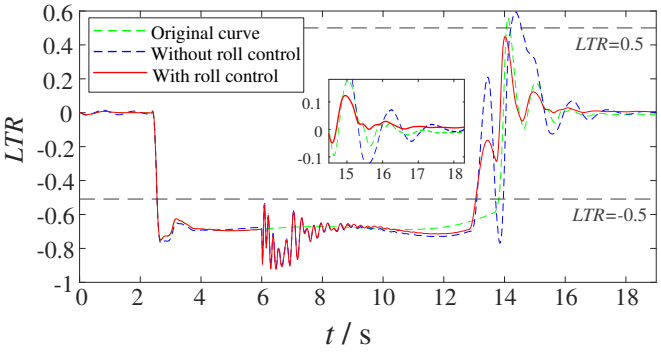

Fig. 13 LTR before/after blowout at t=6s.

range $[3, 14]$s. Obviously, during the process of maneuver, the red curve, where the rollover stability is considered, remains more stable than the dashed blue one. Meanwhile, at the end of the maneuver, the dashed blue curve goes higher than 0.5, which is another dangerous zone, while the red one remains in the range $[-0.5, 0.5]$. All the above discussions validate the control ability and adaptability of the proposed method during tire blowout once again. In addition, all the comparisons of the control results reflect the reliability and availability of the equivalent model.

5 Conclusion

In this paper, an autonomous MPC-based controller for three-axle trucks was proposed to handle the hazard caused by unexpected tire blowout on expressway. By combining the stable-state vehicle dynamic model and the conventional vehicle steering characteristics, an equivalent two-axle chassis was established, through which the control accuracy and the computational load were well balanced at the same time. Based on this equivalent chassis, a high-fidelity tire blowout oriented full vehicle dynamic model was constructed, where the vehicle lateral motion, yaw motion and roll motion were all considered in order to realise real-time accurate path tracking and rollover maintenance simultaneously. Also, a large transient vertical tire force shock was then employed to the front-left tire to simulate the real tire blowout behavior, upon which the MPC-based vehicle controller was designed for effective control. The TruckSim-Simulink co-simulation results illustrated the effectiveness and feasibility of the proposed method.

Future work will concentrate on the experimental validation of the proposed control system and the multi-axle vehicles oriented comprehensive rollover risk evaluation index formulation. In addition, since the vehicle controller is designed based on the linear tire model-based vehicle model, the operating range and performance might will be further expanded by designing a more accurate nonlinear burst tire model, which is also one of our future research topics.

Acknowledgements This work was supported by National Natural Science Foundation of China (NSFC) under Grant U2013601, 61873047, 51975089 and 91948203, and the Program for Innovative Talents in Liaoning Province under Grant LR2020064.

Data availability All data included in this study are available upon request by contact with the corresponding author.

Declarations

Data availability The authors declare that they have no conflict of interest.

References

1. F. Tian, R. Zhou, Z. Li, L. Li, Y. Gao, D. Cao, and L. Chen, "Trajectory planning for autonomous mining trucks considering terrain constraints," *IEEE Transactions on Intelligent Vehicles*, vol. 6, no. 4, pp. 772–786, 2021.
2. P. F. Lima, M. Nilsson, M. Trincavelli, J. Mårtensson, and B. Wahlberg, "Spatial model predictive control for smooth and accurate steering of an autonomous truck," *IEEE Transactions on Intelligent Vehicles*, vol. 2, no. 4, pp. 238–250, 2017.
3. J. Kim, "Truck platoon control considering heterogeneous vehicles," *Applied Sciences*, vol. 10, no. 15, pp. 1–14, 2020.
4. Y. Zhang, A. Khajepour, and M. Ataei, "A universal and reconfigurable stability control methodology for articulated vehicles with any configurations," *IEEE Transac-*

tions on Vehicular Technology, vol. 69, no. 4, pp. 3748–3759, 2020.
5. B. Li, T. Acarman, Y. M. Zhang, L. L. Zhang, C. Yaman, and Q. Kong, "Tractor-trailer vehicle trajectory planning in narrow environments with a progressively constrained optimal control approach," *IEEE Transactions on Intelligent Vehicles*, vol. 5, no. 3, pp. 414–425, 2019.
6. G. Guo and Q. Wang, "Fuel-efficient en route speed planning and tracking control of truck platoons," *IEEE Transactions on Intelligent Transportation Systems*, vol. 20, no. 8, pp. 3091–3103, 2018.
7. A. Sassi, S. Sassi, and F. Tarlochan, "Influence of tire blowout on the collision of a light pickup truck with a guardrail safety barrier," *Proceedings of the Institution of Mechanical Engineers, Part D: Journal of Automobile Engineering*, vol. 234, no. 6, pp. 1714–1724, 2019.
8. X. Sun, H. Zhang, Y. Cai, S. Wang, and L. Chen, "Hybrid modeling and predictive control of intelligent vehicle longitudinal velocity considering nonlinear tire dynamics," *Nonlinear Dynamics*, vol. 97, pp. 1–16, 2019.
9. L. Qi, M. Zhou, and W. Luan, "A dynamic road incident information delivery strategy to reduce urban traffic congestion," *IEEE/CAA Journal of Automatica Sinica*, vol. 5, no. 5, pp. 934–945, 2018.
10. J. Ding and K. Guo, "Development of a generalised equivalent estimation approach for multi-axle vehicle handling dynamics," *Vehicle System Dynamics*, vol. 54, no. 1, pp. 20–57, 2016.
11. A. Soltani, A. Goodarzi, M. H. Shojaeefard, and A. Khajepour, "Vehicle dynamics control using an active third-axle system," *Vehicle System Dynamics*, vol. 52, no. 11, pp. 1541–1562, 2014.
12. Z. Jin, J. Li, Y. Huang, and A. Khajepour, "Study on rollover index and stability for a triaxle bus," *Chinese Journal of Mechanical Engineering*, vol. 32, no. 4, pp. 1–15, 2019.
13. Y. Zhang, A. Khajepour, and Y. Huang, "Multi-axle/articulated bus dynamics modeling: a reconfigurable approach," *Vehicle System Dynamics*, vol. 56, no. 9, pp. 1315–1343, 2018.
14. D. Williams, "On the equivalent wheelbase of a three-axle vehicle," *Vehicle System Dynamics*, vol. 49, no. 9, pp. 1521–1532, 2011.
15. Y. Zhang, Y. Huang, H. Wang, and A. Khajepour, "A comparative study of equivalent modelling for multi-axle vehicle," *Vehicle System Dynamics*, vol. 56, no. 3, pp. 443 – 460, 2018.
16. S. Lu, M. Lian, Z. Cao, T. Zheng, Y. Xiao, X. Chen, and Y. Ma, "Active rectifying control of vehicle with tire blowout based on adaptive fuzzy proportional-integral-derivative control," *Advances in Mechanical Engineering*, vol. 11, no. 3, pp. 1–13, 2019.
17. P. Sathishkumar, R. Wang, L. Yang, and J. Thiyagarajan, "Trajectory control for tire burst vehicle using the standalone and roll interconnected active suspensions with safety-comfort control strategy," *Mechanical Systems and Signal Processing*, vol. 142, no. 2, pp. 1–18, 2020.
18. J. Ji, A. Khajepour, W. W. Melek, and Y. Huang, "Path planning and tracking for vehicle collision avoidance based on model predictive control with multiconstraints," *IEEE Transactions on Vehicular Technology*, vol. 66, no. 2, pp. 952–964, 2017.
19. J. Guo, Y. Luo, and K. Li, "Dynamic coordinated control for over-actuated autonomous electric vehicles with nonholonomic constraints via nonsingular terminal sliding mode technique," *Nonlinear Dynamics*, vol. 85, pp. 583–597, 2016.
20. M. Yue, B. Liu, C. An, and X. Sun, "Extended state observer-based adaptive hierarchical sliding mode control for longitudinal movement of a spherical robot," *Nonlinear Dynamics*, vol. 78, pp. 1233–1244, 2014.
21. W. Zhao, Y. Liu, and L. Liu, "Observer-based adaptive fuzzy tracking control using integral barrier lyapunov functionals for a nonlinear system with full state constraints," *IEEE/CAA Journal of Automatica Sinica*, vol. 8, no. 3, pp. 617–627, 2021.
22. W. Li, Z. Xie, P. K. Wong, X. Mei, and J. Zhao, "Adaptive-event-trigger-based fuzzy nonlinear lateral dynamic control for autonomous electric vehicles under insecure communication networks," *IEEE Transactions on Industrial Electronics*, vol. 68, no. 3, pp. 2447–2459, 2021.
23. Y. Huang, H. Wang, A. Khajepour, H. Ding, K. Yuan, and Y. Qin, "A novel local motion planning framework for autonomous vehicles based on resistance network and model predictive control," *IEEE Transactions on Vehicular Technology*, vol. 69, no. 1, pp. 55–66, 2020.
24. Y. Q. Zhang, Y. J. Liu, Z. F. Wang, R. Bai, and L. Liu, "Neural networks-based adaptive dynamic surface control for vehicle active suspension systems with time-varying displacement constraints," *Neurocomputing*, vol. 408, pp. 176–187, 2020.
25. F. Wang, H. Chen, L. Guo, and Y. Hu, "Predictive safety control for road vehicles after a tire blowout," *Science China Information Sciences*, vol. 61, no. 7, pp. 1–3, 2018.
26. C. Hu and J. Wang, "Trust-based and individualizable adaptive cruise control using control barrier function approach with prescribed performance," *IEEE Transactions on Intelligent Transportation Systems*, pp. 1–11, 2021.
27. Y. Xia, D. Wu, and L. Ping, "Simulation analysis of trajectory control of tire bursting vehicles based on MPC," *2020 5th International Conference on Mechanical, Control and Computer Engineering (ICMCCE)*, pp. 796–801, 2020.
28. M. Yue, L. Yang, H. Zhang, and G. Xu, "Automated hazard escaping trajectory planning/tracking control framework for vehicles subject to tire blowout on expressway," *Nonlinear Dynamics*, vol. 98, no. 1, pp. 1–14, 2019.
29. K. Liu, J. Gong, A. Kurt, H. Chen, and U. Ozguner, "Dynamic modeling and control of high-speed automated vehicles for lane change maneuver," *IEEE Transactions on Intelligent Vehicles*, vol. 3, no. 3, pp. 329–339, 2018.
30. H. Guo, F. Wang, H. Chen, and D. Guo, "Stability control of vehicle with tire blowout using differential flatness based MPC method," *Proceedings of the 10th World Congress on Intelligent Control and Automation*, pp. 2066–2071, 2012.
31. L. Yang, M. Yue, J. Wang, and W. Hou, "RMPC-Based Directional Stability Control for Electric Vehicles Subject to Tire Blowout on Curved Expressway," *ASME Transactions on Journal of Dynamic Systems, Measurement*, vol. 141, no. 4, pp. 1–9, 2018.
32. K. Liu, J. Gong, S. Chen, Y. Zhang, and H. Chen, "Model predictive stabilization control of high-speed autonomous ground vehicles considering the effect of road topography," *Applied Sciences*, vol. 8, no. 5, pp. 1–16, 2018.
33. Y. Zhang, Y. Huang, H. Wang, and A. Khajepour, "A comparative study of equivalent modelling for multi-axle vehicle," *Vehicle System Dynamics*, vol. 56, no. 3, pp. 443–460, 2017.

34. C. Hu, Z. Wang, Y. Qin, Y. Huang, J. Wang, and R. Wang, "Lane keeping control of autonomous vehicles with prescribed performance considering the rollover prevention and input saturation," *IEEE Transactions on Intelligent Transportation Systems*, vol. 21, no. 7, pp. 3091–3103, 2020.
35. K. Liu, J. Gong, S. Chen, Y. Zhang, and H. Chen, "Dynamic modeling analysis of optimal motion planning and control for high-speed self-driving vehicles," *Journal of Mechanical Engineering*, vol. 54, no. 14, pp. 141–151, 2018.
36. H. Imine and M. Djemai, "Switched control for reducing impact of vertical forces on road and heavy-vehicle rollover avoidance," *IEEE Transactions on Vehicular Technology*, vol. 65, no. 6, pp. 4044–4052, 2016.
37. G. Phanomchoeng and R. Rajamani, "New rollover index for the detection of tripped and untripped rollovers," *IEEE Transactions on Industrial Electronics*, vol. 60, no. 10, pp. 4726–4736, 2013.
38. S. Patwardhan, H. Tan, and M. Tomizuka, "Experimental results of tire burst controller for AHS," *IFAC Proceedings Volumes*, vol. 29, no. 1, pp. 7885–7890, 1996.
39. K. Guo, J. Huang, and X. Song, "Analysis and control of vehicle movement with blown-out tire," *Automotive Engineering*, vol. 29, no. 12, pp. 1041–1045, 2007.
40. L. Yang, M. Yue, H. Zhang, and G. Xu, "Toward hazard reduction of road vehicle after tire blowout: A driver steering assist control strategy," *2019 Chinese Control Conference (CCC)*, pp. 6600–6605, 2019.